ISSN 0965-5425, Computational Mathematics and Mathematical Physics, 2016, Vol. 56, No. 6, pp. 1034–1047. © Pleiades Publishing, Ltd., 2016.
Original Russian Text © V.A. Gushchin, P.V. Matyushin, 2016, published in Zhurnal Vychislitel'noi Matematiki i Matematicheskoi Fiziki, 2016, Vol. 56, No. 6, pp. 1049–1063.

Dedicated to the memory of O.M. Belotserkovskii

Simulation and Study of Stratified Flows around Finite Bodies

V. A. Gushchin and P. V. Matyushin

Institute for Computer-Aided Design, Russian Academy of Sciences,
ul. Vtoraya Brestskaya 19/18, Moscow, 123056 Russia
e-mail: gushchin47@mail.ru, pmatyushin@mail.ru

Received November 9, 2015

Abstract—The flows past a sphere and a square cylinder of diameter d moving horizontally at the velocity U in a linearly density-stratified viscous incompressible fluid are studied. The flows are described by the Navier–Stokes equations in the Boussinesq approximation. Variations in the spatial vortex structure of the flows are analyzed in detail in a wide range of dimensionless parameters (such as the Reynolds number $\mathrm{Re} = Ud/\nu$ and the internal Froude number $\mathrm{Fr} = U/(Nd)$, where ν is the kinematic viscosity and N is the buoyancy frequency) by applying mathematical simulation (on supercomputers of Joint Supercomputer Center of the Russian Academy of Sciences) and three-dimensional flow visualization. At $0.005 < \mathrm{Fr} < 100$, the classification of flow regimes for the sphere (for $1 < \mathrm{Re} < 500$) and for the cylinder (for $1 < \mathrm{Re} < 200$) is improved. At $\mathrm{Fr} = 0$ (i.e., at $U = 0$), the problem of diffusion-induced flow past a sphere leading to the formation of horizontal density layers near the sphere's upper and lower poles is considered. At $\mathrm{Fr} = 0.1$ and $\mathrm{Re} = 50$, the formation of a steady flow past a square cylinder with wavy hanging density layers in the wake is studied in detail.

Keywords: stratified viscous liquid, sphere, cylinder, diffusion, unsteady internal waves, mathematical simulation.

DOI: 10.1134/S0965542516060142

INTRODUCTION

The flow patterns around a finite body in river and sea water differ widely. Only a wake behind the body is observed in river water, while the flow pattern in sea water additionally involves internal waves, which considerably complicate the situation. This phenomenon is explained by the fact that the density of fresh water in rivers and lakes remains nearly unchanged, while the density sea (salty) water increases with depth, which gives rise to buoyancy. According to the linear theory, the length of internal waves in a vertical plane is given by $\lambda = 2\pi \mathrm{Fr} d$ (see [1]). Approximate classifications of flow regimes for a sphere and a circular cylinder (of diameter d) moving horizontally at the constant velocity U in stratified sea water were obtained experimentally in [2–10]. More specifically, results for a sphere for ($0.005 < \mathrm{Fr} < 20$, $5 < \mathrm{Re} < 10000$), ($0.125 < \mathrm{Fr} < 6.35$, $150 < \mathrm{Re} < 50000$), and ($0.01 < \mathrm{Fr} < 10$, $7 < \mathrm{Re} < 3000$) are presented in [2–4], respectively; while results for a circular cylinder for ($0.02 < \mathrm{Fr} < 13$, $5 < \mathrm{Re} < 4000$), ($0.001 < \mathrm{Fr} < 3$, $10 < \mathrm{Re} < 1300$), and ($0.01 < \mathrm{Fr} < 1.5$, $15 < \mathrm{Re} < 2000$) can be found in [8–10], respectively. The experimental study in [4] includes the results of [5–7]. With the help of mathematical simulation, transitions between flow regimes can be analyzed in detail and the classification of 3D separated flows of a linearly density-stratified incompressible viscous (SIV) fluid around a sphere and a cylinder can be improved.

Based on computations, our schematic classification of SIV flow regimes around a sphere (see Fig. 1) is more similar to the classification presented in [2]. Inspection of Fig. 1 reveals that the flow regimes exhibit a strong dependence on Re for $\mathrm{Fr} > 1$ and on Fr for $\mathrm{Fr} < 1$ (at moderate $50 < \mathrm{Re} < 500$). This result is confirmed in [3], while, in the experimental study [4], the flow regimes for $\mathrm{Fr} < 1$ depend on both Fr and Re. Thus, the experimental data from [2–7] agree poorly with each other. A more detailed comparison of our results with the experiments in [2–10] will be made after describing our results.

There are few works concerning the mathematical simulation of SIV flows past a sphere and a cylinder. For example, results for a sphere at $\mathrm{Re} = 200$ and $0.125 < \mathrm{Fr} < 100$ were presented in [11]. They agree well with [2], except for small $\mathrm{Fr} < 0.25$, at which an unsteady periodic flow is observed in the sphere wake in

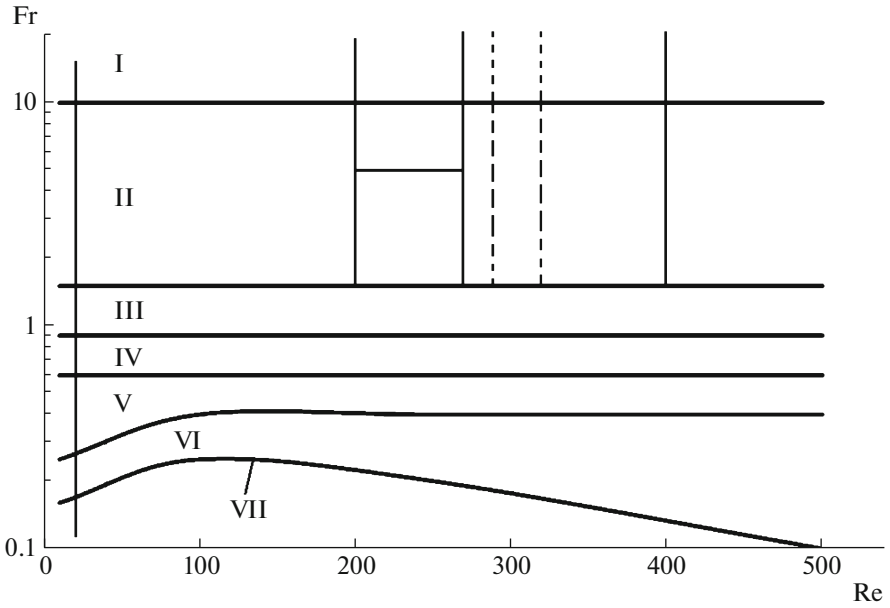

Fig. 1. Classifications of SIV flow regimes past a sphere.

[2], in contrast to a steady flow in [11]. In [12–14], we describe the numerical solution of this problem at Re = 100 and 0.005 < Fr < 100, which agrees well with [2]. In this paper, in addition to Re = 100, we present results for Re = 10, 200, and 250.

In the mathematical simulation of sphere flows, it has been found that the grid has to be refined in the crests of internal waves in the path of the sphere's center. The spherical grid used in our computations is not suitable for this purpose, so the circular cylinder with a cylindrical grid was replaced by a square cylinder (or a square prism) with a square cross section rather than a circular one. Accordingly, we used a Cartesian grid, which could easily be refined in crests of internal waves in the path of the cylinder's central axis. However, comparisons had to be made with experimental results obtained for a circular cylinder [8–10]. Obtained in this work, the classification of SIV flow regimes behind a square cylinder at Re < 200 with original names used for flow regimes (see Fig. 7) is in certain agreement with experimental works [8–10]. The most interesting are the wake flows with wavy hanging density layers observed at Fr < 0.37 and Re > 30. The formation of such flows and their steady states are examined in detail at Fr = 0.1 and Re = 50. Moreover, we refute the experimental result of [10] that the normal velocities on the upper and lower edges of discontinuities (of hanging density layers) differ.

1. FORMULATION OF THE PROBLEM AND SOLUTION METHOD

The density $\rho(x, y, z) = 1 - \frac{x}{2A} + S(x, y, z)$ of a linearly stratified fluid is nondimensionalized by the density ρ_0 at the level of the body center. Here, (x, y, z) are Cartesian coordinates with the origin placed at the center of the sphere, the x axis is directed vertically upward, the z axis is parallel to the free-stream velocity U, (x, y, z) are nondimensionalized by $d/2$, $A = \Lambda/d$ is the scale ratio, Λ is the buoyancy scale, $N = \sqrt{g/\Lambda}$ is the buoyancy frequency, $T_b = 2\pi/N$ is the buoyancy period, $\mathbf{g}$ is the acceleration of gravity, and S is the salinity perturbation, including the salt compression coefficient $\beta = \frac{1}{\rho_0}\left(\frac{\partial \rho}{\partial S}\right)_p$. The Navier–Stokes equations in the Boussinesq approximation have the form

$$\frac{\partial S}{\partial t} + (\mathbf{v} \cdot \nabla)S = \frac{2}{\mathrm{Sc} \cdot \mathrm{Re}}\Delta S + \frac{v_x}{2A}, \tag{1}$$

$$\frac{\partial \mathbf{v}}{\partial t} + (\mathbf{v} \cdot \nabla)\mathbf{v} = -\nabla p + \frac{2}{\mathrm{Re}}\Delta \mathbf{v} + \frac{A}{2\mathrm{Fr}^2} S \frac{\mathbf{g}}{g}, \tag{2}$$

$$\nabla \cdot \mathbf{v} = 0, \tag{3}$$

where $\mathbf{v} = (v_x, v_y, v_z)$ is the velocity, p is the pressure minus hydrostatic pressure (nondimensionalized by $\rho_0 U^2$), $\mathrm{Sc} = \nu/k_s$ is the Schmidt number, k_s is the diffusion coefficient of salt, t is time (nondimensionalized by the characteristic time $t_0 = d/(2U) = 1/(2\mathrm{Fr}N)$), ∇ is the Hamiltonian operator, and Δ is the Laplacian. It is convenient to introduce another time T nondimensionalized by the buoyancy period: $T = tt_0/T_b = [t/(2\mathrm{Fr}N)]N/2\pi = t/(4\pi\mathrm{Fr})$. The parameter $A > 100$ was chosen so as to satisfy the conditions $N \approx 1\ \mathrm{s}^{-1}$ and $0.1\ \mathrm{cm} < d < 10\ \mathrm{cm}$, which hold in the experiments.

In the case of a sphere flow, Eqs. (1)–(3) are written in spherical coordinates R, θ, and φ ($x = R\sin\theta\cos\varphi$, $y = R\sin\theta\sin\varphi$, $z = R\cos\theta$). Let u, v, and w be the components of the velocity $\mathbf{v}$ in the directions R, θ, and φ, respectively. On the solid surface of the sphere, we specified the no-slip boundary conditions $v = 0$ and $w = 0$ and the no-flow conditions $u = 0$ and $\left.\frac{\partial\rho}{\partial R}\right|_{R=1} = 0$ (i.e., $\left.\left(\frac{\partial S}{\partial R} - \frac{1}{2A}\frac{\partial x}{\partial R}\right)\right|_{R=1} = 0$ or $\left.\frac{\partial S}{\partial R}\right|_{R=1} = \frac{\sin\theta\cos\varphi}{2A}$). On the outer boundary of the computational domain, for $z < 0$, we specified the unperturbed flow: $u = \cos\theta$, $v = -\sin\theta$, $S = 0$, and $w = 0$; while $u = \cos\theta$, $v = -\sin\theta$, $S = 0$, and $\frac{\partial w}{\partial R} = 0$ were set for $z \geqslant 0$.

The problem was solved on a uniform grid in r, θ, and φ defined as $\Omega = \{r_i = i\Delta r = ir_{\max}/N,\ R_i = 1 + \frac{i}{N_0}\sqrt{\frac{2}{\mathrm{Re}}} + r_i^m,\ i = 0, 1, 2, \ldots, N;\ \theta_j = j\Delta\theta = \pi j/M, j = 0, 1, 2, \ldots, M;\ \varphi_k = k\Delta\varphi = 2\pi k/L,\ k = 0, 1, 2, \ldots, L\}$, where N is the total number of grid cells in the radial direction and N_0 is the number of grid cells lying within the boundary layer of thickness $\delta = \sqrt{\frac{2}{\mathrm{Re}}}$. The computations were performed on a grid with the number of nodes given by $N \times M \times L = 240 \times 60 \times 120 = 1728\,000$. In all computations in this work, we set $m = 3$ and $r_{\max} = 3$, so the outer boundary of the computational domain was the distance $R_N \approx 14.5d$ away from the center of the sphere.

The problem was solved using the method MERANZH of splitting with respect to physical factors for an incompressible fluid with an explicit hybrid finite-difference scheme used to approximate the convective terms in Eqs. (1)–(3) [15, 16].

Suppose that the velocity and pressure fields are known at some time $t_n = n\tau$, where τ is the time step and n is the number of steps. Then the scheme for finding the unknown functions at the time $t_{n+1} = (n+1)\tau$ can be represented in the form

$$\frac{S^{n+1} - S^n}{\tau} = -(\mathbf{v}^n \cdot \nabla)S^n + \frac{2}{\mathrm{Sc} \cdot \mathrm{Re}}\Delta S^n + \frac{v_x^n}{2A}, \tag{4}$$

$$\frac{\tilde{\mathbf{v}} - \mathbf{v}^n}{\tau} = -(\mathbf{v}^n \cdot \nabla)\mathbf{v}^n + \frac{2}{\mathrm{Re}}\Delta\mathbf{v}^n + \frac{A}{2\mathrm{Fr}^2}S^{n+1}\frac{\mathbf{g}}{g}, \tag{5}$$

$$\tau\Delta p = \nabla \cdot \tilde{\mathbf{v}}, \tag{6}$$

$$\frac{\mathbf{v}^{n+1} - \tilde{\mathbf{v}}}{\tau} = -\nabla p. \tag{7}$$

On Ω we define grid functions $u_{i,j,k}^n$, $v_{i,j,k}^n$, $w_{i,j,k}^n$, $S_{i,j,k}^n$, and $p_{i,j,k}^n$ such that the velocity components $u_{i,j,k}^n$, $v_{i,j,k}^n$, and $w_{i,j,k}^n$ coincide with the sought functions u, v, and w at the midpoints of grid cell faces, while the salinity and pressure perturbations, i.e., $S_{i,j,k}^n$ and $p_{i,j,k}^n$ coincide with the sought functions S and p at the centers of cells (i.e., a staggered stencil is used). The Laplacian operators in Eqs. (4)–(6) are approximated by central differences. The Poisson equation (6) for pressure is solved by applying the conjugate gradient method with diagonal preconditioning. The convective terms in Eqs. (4) and (5) are written in conservative form (with the use of Eq. (3)) as

$$\frac{\partial f}{\partial t} + \frac{1}{R'}\frac{\partial(uf)}{\partial r} + \cdots, \quad \text{where} \quad f = u, v, w, S, \quad R' = \frac{dR}{dr}. \tag{8}$$

By analogy with the one-dimensional linear case, we consider the explicit hybrid scheme from [15, 16] as applied to the approximation of Eq. (8):

$$\frac{f_{i,j,k}^{n+1} - f_{i,j,k}^{n}}{\tau} + \frac{u_{i+1/2,j,k}^{n} f_{i+1/2,j,k}^{n} - u_{i-1/2,j,k} f_{i-1/2,j,k}^{n}}{(R')_i \Delta r} + \cdots.$$

In the term $u_{i\pm1/2,j,k}^{n} f_{i\pm1/2,j,k}^{n}$, the velocity $u_{i\pm1/2,j,k}^{n}$ is determined at points lying a distance of $0.5\Delta r$ away from the location point of $f_{i,j,k}^{n}$.

With the indices j and k dropped, the formula for approximating $f_{i+1/2,j,k}$ is written as

$$f_{i+1/2}^{n} = \begin{cases} \alpha f_{i-1}^{n} + (1-\alpha-\beta) f_i^{n} + \beta f_{i+1}^{n}, & u_{i+1/2} \geq 0, \\ \alpha f_{i+2}^{n} + (1-\alpha-\beta) f_{i+1}^{n} + \beta f_i^{n}, & u_{i+1/2} < 0, \end{cases}$$

here, if $(u\Delta f \Delta^2 f)_{i+1/2}^{n} \geq 0$, then we use the scheme with $\beta = 0$ and $\alpha = -0.5(1 - C_{i+1/2})$, where $C_{i+1/2} = \tau|u_{i+1/2}|/\Delta r$ is the Courant number, while, if $(u\Delta f \Delta^2 f)_{i+1/2}^{n} < 0$, then we use the scheme with $\alpha = 0$ and $\beta = 0.5(1 - C_{i+1/2})$, where $\Delta f_{i+1/2}^{n} = f_{i+1}^{n} - f_i^{n}$ and $\Delta^2 f_{i+1/2}^{n} = \Delta f_{i+1}^{n} - \Delta f_i^{n}$.

As a result, the convective terms in Eqs. (4) and (5) are approximated using an explicit hybrid finite-difference scheme (combining a modified central difference scheme (for $\alpha = 0$) with a modified upwind difference scheme (for $\beta = 0$) and having the local switching condition $(u\Delta f \Delta^2 f)_{i+1/2}^{n}$, which depends on the signs of the velocity and the first and second differences (derivatives) in each of the coordinate directions). The scheme is second-order accurate in space, monotone, has minimum numerical viscosity and dispersion, and performs in a wide range of the Reynolds and Froude numbers.

2. VISUALIZATION OF VORTEX STRUCTURES IN THE WAKE BEHIND A SPHERE

To gain insight into the dynamics and mechanisms of vortex shedding in the wake of a sphere moving in an incompressible viscous fluid, it is not sufficient to use three well-known intuitive vortex indicators (pressure minimum, streamlines, and vorticity level surfaces). For example, in the simplest case of an axisymmetric flow past a sphere at $\mathrm{Re} = 100$, two vortex structures can be identified in the wake: a vortex ring in the recirculation zone of the wake (RZ) and a vortex shell enclosing the ring [17–23] (Fig. 2a). At the same time, the streamlines in a frame of reference tied to the sphere visualize only the ring, the contour lines of the vorticity $\boldsymbol{\omega} = 0.5\mathrm{curl}\,\mathbf{v}$ reveal only the shell, while the lines of constant pressure do not visualize anything at all [17–23]. Similarly, for a three-dimensional flow of complex geometry, the level surfaces of the modulus of vorticity show only some of the vortex structures occurring in the flow. Accordingly, special flow visualization techniques have been proposed that identify most of the vortices in a wake. Let us briefly describe two of them.

For a fixed point in the flow field, we examine the behavior of a streamline in Cartesian coordinates $\mathbf{x} = (x, y, z)$ that begins at this point and moves at the velocity of this point. In a neighborhood of this point $(0, 0, 0)$, in the linear approximation, we can write $\mathbf{v} = d\mathbf{x}/dt \approx \mathbf{G}\mathbf{x}$, where $\mathbf{G}$ is the velocity gradient tensor ($\mathrm{G}_{ij} = \mathrm{v}_{i,j} = \partial v_i/\partial x_j$). If σ_1 and σ_2 are two complex conjugate eigenvalues of $\mathbf{G}$, i.e., $\sigma_1 = \alpha - i\beta$ and $\sigma_2 = \alpha + i\beta$ (where $\beta = \mathrm{Im}(\sigma_{1,2}) > 0$), then, according to the theory of ordinary differential equations, we can choose two corresponding complex conjugate eigenvectors $0.5(\mathbf{h}_1 \pm i\mathbf{h}_2)$, where $\mathbf{h}_1$ and $\mathbf{h}_2$ are real vectors lying in a single plane, in which the phase trajectories are either closed ovals centered at the fixed point (for $\alpha = 0$) or spiral curves with a focus at this point. This means that there is a vortex at this point (see [24, pp. 119–122]). Moreover, the angular velocity of the fluid rotating about this fixed point is equal to β. For this reason, the core of a vortex flow is defined as the collection of flow subregions where the velocity gradient tensor has complex conjugate eigenvalues [25] (see the level surfaces of β in Fig. 3).

In [26] the core of a vortex flow was defined as the collection of flow subregions where the second eigenvalue of the tensor $\mathbf{S}^2 + \boldsymbol{\Omega}^2$ is negative ($\lambda_2 < 0$, Fig. 2); here, $\mathbf{S}$ and $\boldsymbol{\Omega}$ are the symmetric and antisymmetric parts of $\mathbf{G}$ ($S_{ij} = 0.5(v_{i,j} + v_{j,i})$ is the strain rate tensor, $\Omega_{ij} = 0.5(v_{i,j} - v_{j,i})$ is the vorticity tensor, and the symmetric tensor $\mathbf{S}^2 + \boldsymbol{\Omega}^2$ has three real eigenvalues $\lambda_1 \geqslant \lambda_2 \geqslant \lambda_3$). A good performance of β- and λ_2-visualizations was demonstrated in [18–23].

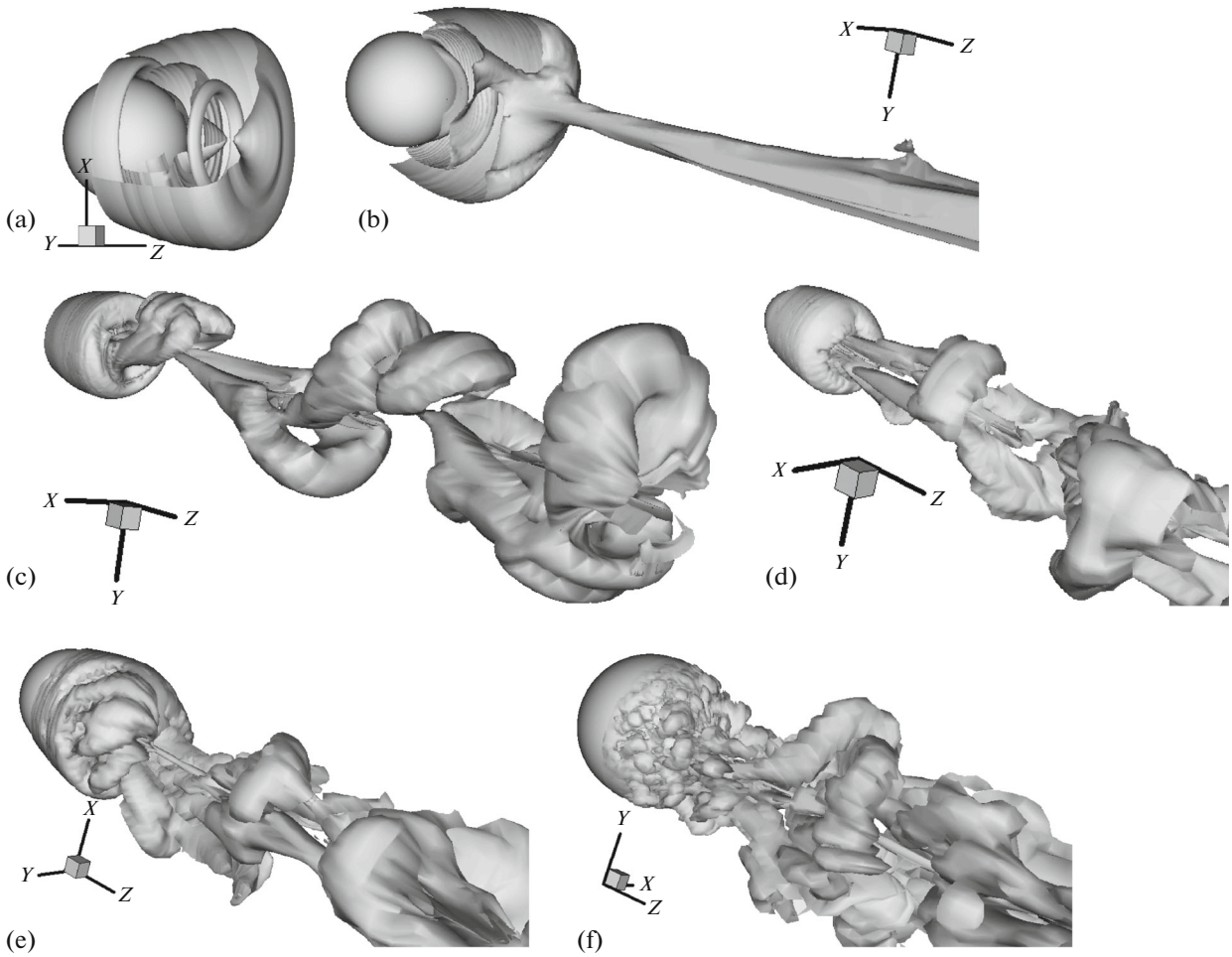

Fig. 2. Vortex structures of the wake behind a sphere at Fr = ∞: (a–f) Re = 200, 250, 350, 700, 10^4, and 5×10^5; and (a)–(f) $\lambda_2 = -10^{-6}$ and −0.16, -2×10^{-5}, -2×10^{-5}, -10^{-4}, -10^{-4}, and -10^{-4}.

3. CLASSIFICATION OF SIV FLOW REGIMES PAST A SPHERE FOR $1 < \mathrm{Re} < 5 \times 10^2$

At Fr > 10, flow regimes typical of a homogeneous fluid are observed (regime I, homogeneous, Fig. 2): at Re = 20.5, an axisymmetric flow separation from the sphere begins (Fig. 2a); at Re = 200, the axial symmetry in RZ is lost, but the flow remains steady up to Re = 270 (Figs. 2b, 3a); for 270 < Re ⩽ 400, vortex loops of the same orientation are periodically formed in RZ; and, starting at Re = 400, vortex loops are formed with alternating oppositely directed orientations [21–23]. In [23], the basic mechanisms of vortex formation in the wake behind a sphere were identified for the first time on the basis of β-visualization. Moreover, a chain of mechanisms characterizing a particular flow regime was composed. Due to this detailed description of vortex formation mechanisms in the wake behind a sphere, for 290 < Re < 320, a new subregime of periodic unsteady flow (270 < Re ⩽ 400) was discovered in [23], while it was previously believed that the flow regime at 270 < Re ⩽ 400 is divided into only two subregimes: (a) 270 < Re < 290 (wavy two-thread wake) and (b) 290 < Re ⩽ 400. The basic differences between subregimes (a) 270 < Re < 290, (a1) 290 < Re < 320, and (b) 320 < Re ⩽ 400 are observed in the mechanism of vortex formation in RZ [23].

As Fr decreases from 10 to 1.5, regime II (quasi-homogeneous) is observed: the above subregimes of regime I are flattened in the vertical and horizontal directions, and four vortex threads connected to a vortex shell enclosing RZ play a dominant role in the wake (Fig. 3b). At Fr < 1.5, there are five "stratified" flow regimes III–VII, which differ substantially from I and II. Specifically, internal waves with a wavelength $\lambda/d \approx 2\pi\mathrm{Fr}$ dominate in the flow. The topology of the flow depends strongly on Fr, but varies slightly with growing Re (Fig. 1). Below, the flow regimes for Fr < 1.5 are indicated and the corresponding approximate ranges of Fr for 80 < Re < 120 are given: regime III, nonaxisymmetric associated vortex in

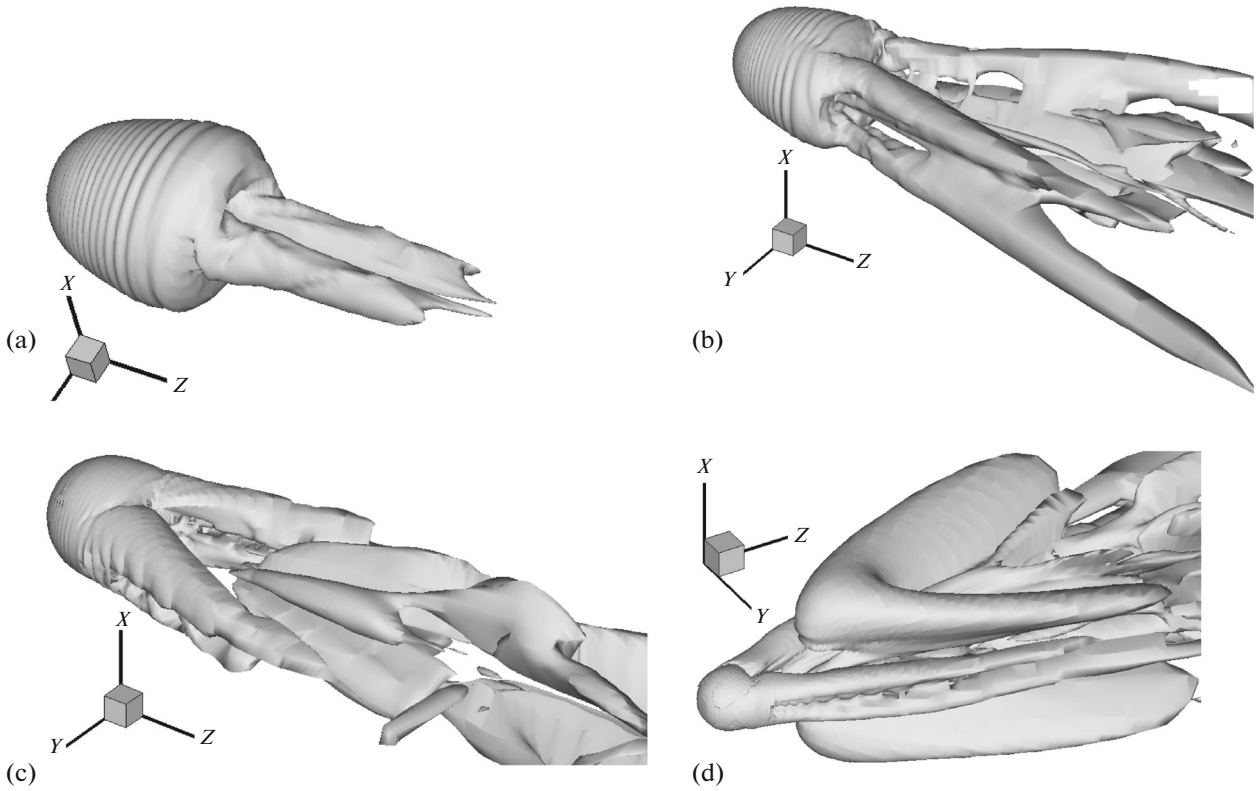

Fig. 3. (a)–(d) Vortex structure of the wake behind a sphere at (Fr, Re) = (100, 250), (2, 250), (1, 250), and (1, 200): (a) two-thread wake, (b) six-thread wake, and (c, d) four-thread wake ($\beta = 0.04, 0.04, 0.08, 0.02$).

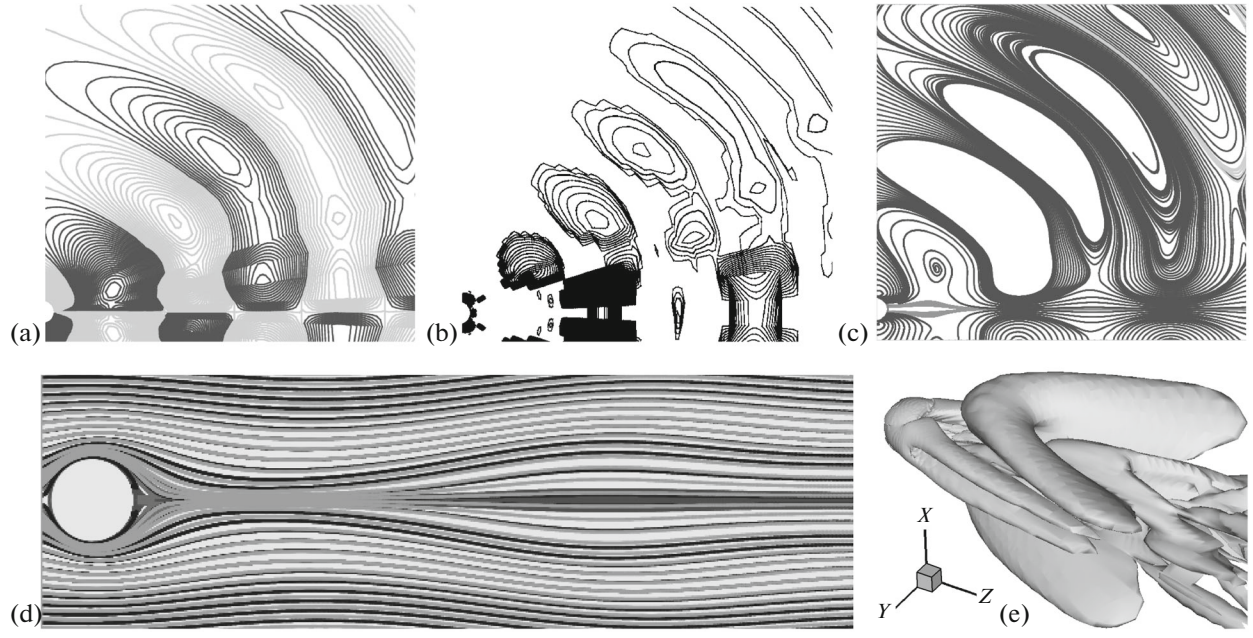

Fig. 4. (a)–(d) Flow patterns past a sphere in a vertical plane and (e) total vortex structure of this flow at Fr = 1 (Re = 100): (a) contour lines of the salinity perturbation S ($\delta S = 5 \times 10^{-6}$, darker lines correspond to negative values of S); (b) contour lines of $\beta > 0$ ($\delta\beta = 0.002$); streamlines in the frames of reference tied to the (c) fluid and (d) sphere; and (e) the level surface of $\beta = 0.02$.

RZ (Figs. 3c, 3d, 4, 5a) ($0.9 < \mathrm{Fr} < 1.5$) (in Fig. 4d, note the wave crests above and below the path of the sphere's center, which approach the sphere with decreasing Fr); regime IV, two symmetric vortex loops in RZ (Fig. 5b) ($0.6 < \mathrm{Fr} \leqslant 0.9$); regime V, the lack of RZ (Figs. 5b, 5c) ($0.4 \leqslant \mathrm{Fr} \leqslant 0.6$); regime VI, a new

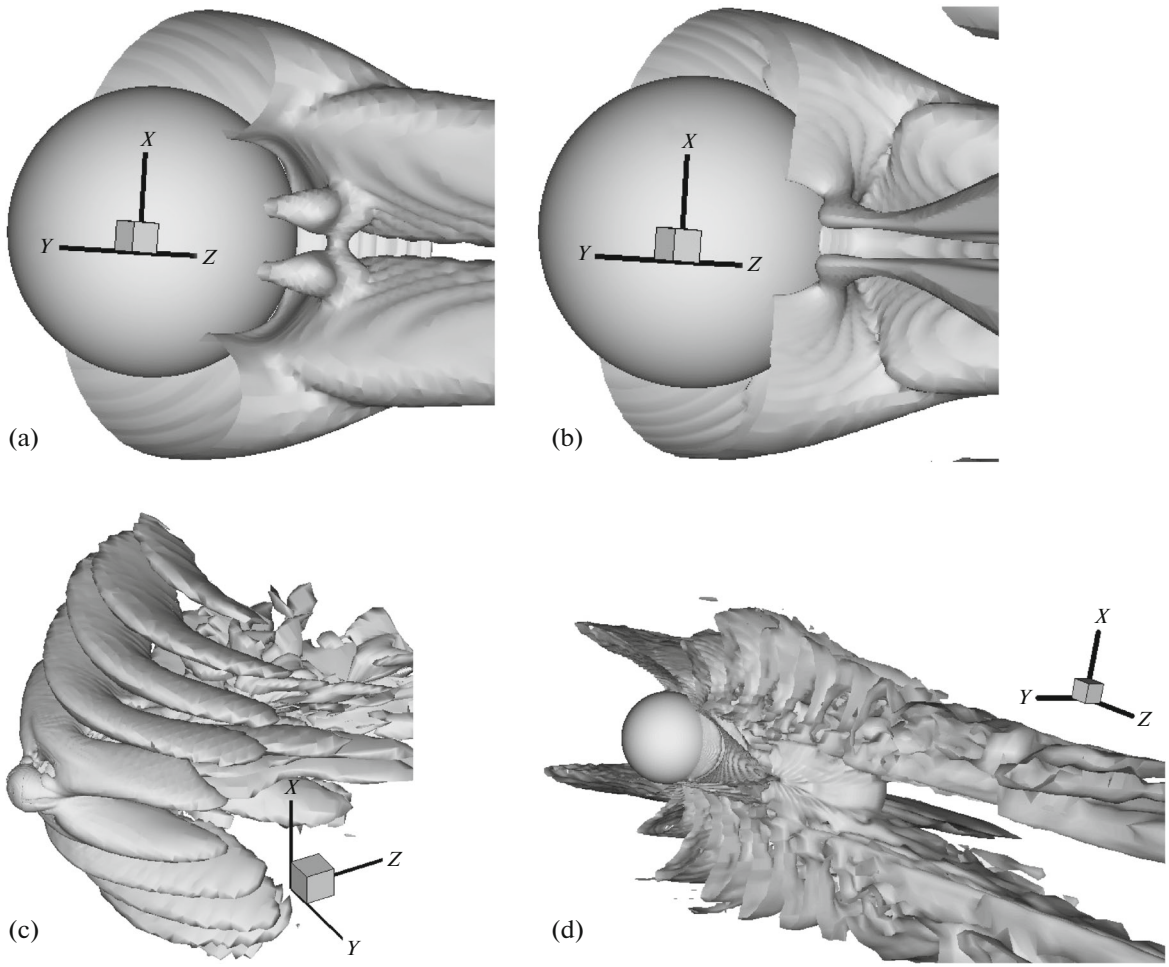

Fig. 5. Vortex structure of the wake behind a sphere at Re = 100: (a–d) Fr = 1, 0.6, 0.5, and 0.08 (β = 0.1, 0.087, 0.02, and 0.005).

RZ is formed from the crests of the associated wave nearest to the sphere ($0.25 < \mathrm{Fr} < 0.4$); and regime VII, vortices with a vertical axis of rotation in the new RZ; they are surrounded by internal waves from above and below (Fig. 5d) ($\mathrm{Fr} \leqslant 0.25$). At $\mathrm{Fr} < 0.3$ and $\mathrm{Re} > 120$, a chain of horizontally oriented vortex loops is formed in the wake.

Figures 4a–4c demonstrates a similarity between the contour lines of S, those of β, and the streamlines in the frame of reference associated with the fluid in a vertical plane. This justifies the fact that the V-shaped vortex structure in Fig. 4e lying above four vortex threads connected to the vortex shell is a part of the spatial vortex structure of density internal waves associated with the wake behind the sphere.

Interestingly, four vortex threads connected to the vortex shell at Fr = 1 in Fig. 4e are transformed into horizontal density layers lying ahead of the sphere in Fig. 5d at Fr = 0.08. As Fr is further decreased to zero (when the sphere ceases to move), there remain only two horizontal pancake density layers near the upper and lower poles of the sphere at rest [27, 28]. In the mathematical simulation of a stationary sphere placed in a stationary viscous stratified diffusive fluid, one of this paper's authors discovered the formation of unsteady diffusion-induced internal waves [27, 28], which lead over time to the formation of the horizontal pancake density layers described above. (If the diffusion term is dropped from Eq. (1), then no horizontal density layers are observed in our numerical experiment.) The simulation in [27, 28] was based on solving the same system (1)–(3), but with the characteristic velocity set to $U = 1$ mm and with the z axis directed upward to take into account the axial symmetry (about the vertical axis) of this slow diffusion flow from the equatorial plane to the poles of the sphere.

Initially, the number of these unsteady internal waves is proportional to T (the number of buoyancy periods T_b having elapsed since the stationary sphere was placed in the stationary fluid). For example, at

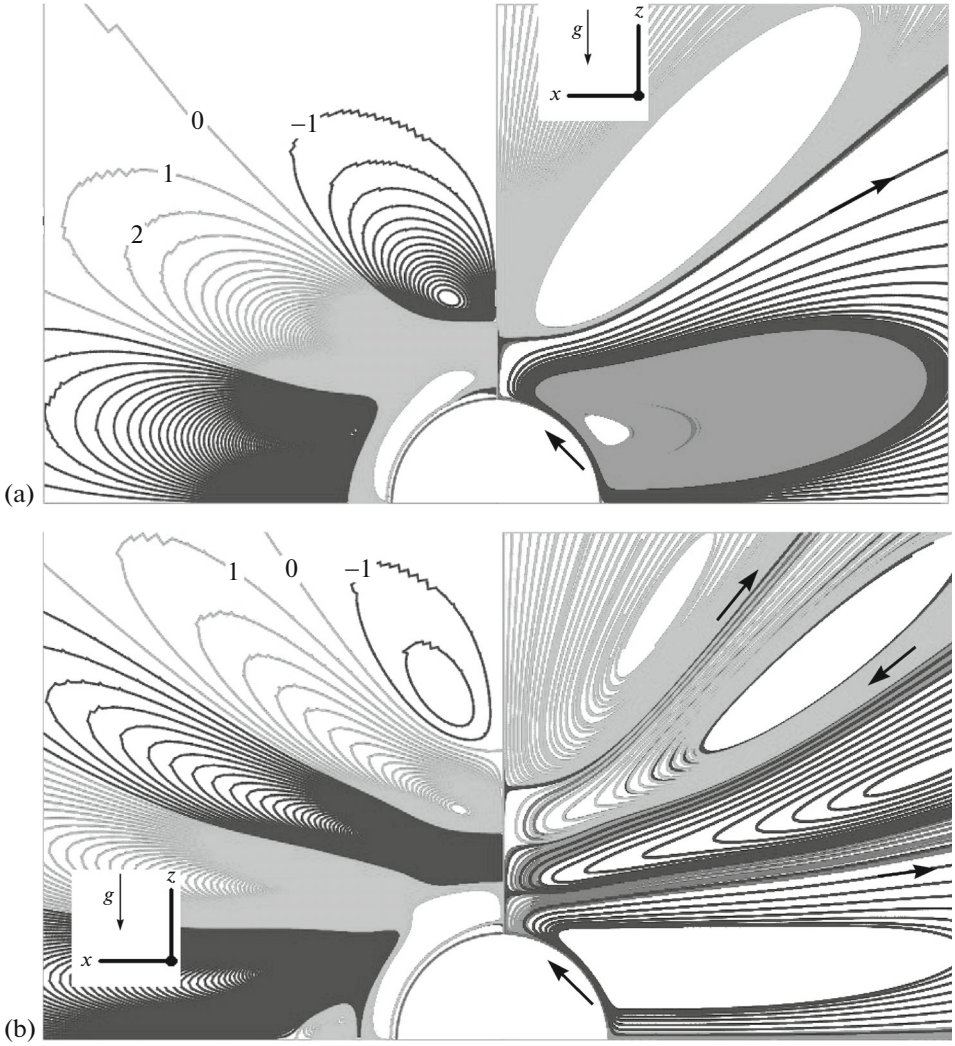

Fig. 6. Evolution of the diffusion-induced flow past a sphere submerged in a continuously stratified fluid ($d = 2$ cm, $T_b = 6.34$ s): (a), (b) contour lines of the horizontal density gradient $\rho_x \equiv S_x$ with a contour interval of 10^{-12} (left panels) and instantaneous streamlines (right panels) at $T = 1, 2$.

$T = 2$, the streamline pattern in vertical planes passing through the vertical axis of symmetry of the sphere contains four ($2T$) convective cells (i.e., two (T) internal waves) above and below the equatorial plane (Fig. 6b). The radius of the main convective cell adjacent to most of the spherical surface is determined by the radius of the sphere. For $T > 37$, the sizes and locations of the convective cells are gradually stabilized. In the upper and lower half-planes, there appear quasi-steady flows in the form of a major convective cell and two thin horizontal convective cells (with a thickness of 2.2 mm) that are adjacent to the major one and pass near the poles of the sphere. Similar processes are observed in the contour lines of the horizontal gradient of the salinity perturbation (Fig. 6). However, $(2T + 1)$ cells are initially observed in each of the half-planes in the contour line pattern. The maximum velocity of this diffusion flow is 0.006 mm/s.

For $\mathrm{Fr} < 0.3$, the computed vertical and horizontal angles of vortex shedding observed at $\mathrm{Re} = 100$ (see [14]) are in good agreement with the results of [2]. For $0.3 < \mathrm{Fr} < 1$, the computed angles are 5–15° smaller than those in [2]. This can be explained by the coarse grid used for $R > 2$, which prevents the adequate resolution of wave crests in the path of the sphere. The drag increment $\Delta C_d(\mathrm{Fr}) = C_\mathrm{d}(\mathrm{Fr}) - C_d(\infty)$ of the sphere computed as a function of Fr at $\mathrm{Re} = 100$ agrees well with the experimental results of [29, 30] for $\mathrm{Fr} > 0.05$ (see [14]).

For $\mathrm{Re} < 21$, the topology of flow regimes III–V and VII simplifies significantly, because they do not contain RZ. At $\mathrm{Re} = 10$, for example, regime VI with RZ is observed for $1.6 < \mathrm{Fr} \leqslant 0.25$. For

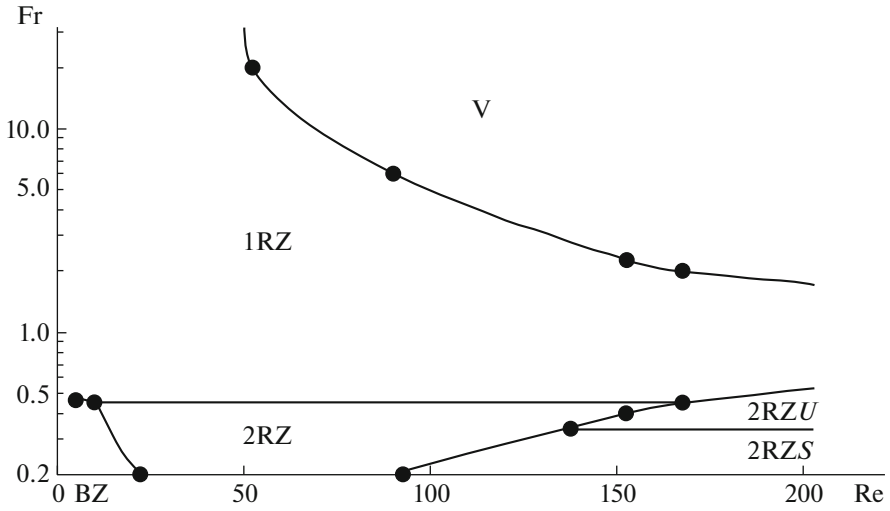

Fig. 7. Classifications of SIV flow regimes past a square cylinder.

Fr < 1, ΔC_d(Fr) at Re = 10 is two to six times larger than that for 100 < Re < 500 (ΔC_d = 1.461, 1.546, 1.626, 1.816, 1.783, 1.481, 0.628, 0.076, –0.179, and –0.164 at Fr = 0.004, 0.05, 0.1, 0.2, 0.3, 0.4, 0.6, 0.8, 1.0, and 2.0, respectively).

Joining two close classifications of flow regimes presented in [2, 3], we obtain the following five flow regimes for moderate values of Re (150 < Re < 300): (1) 3 < Fr < 6.35, a quasi-homogeneous regime with flow patterns typical of a homogeneous fluid; (2) 0.75 < Fr < 3, a transitional regime; (3) 0.4 < Fr < 0.75, distinct internal waves; (4) 0.23 < Fr < 0.4, the instability of internal waves; and (5) 0 < Fr < 0.23, quasi-two-dimensional vortices with a vertical axis of rotation bounded above and below by internal waves. Thus, our classification is similar to the experimental results in [2, 3].

The following regimes were obtained at Re = 100 in [4]: (A) a wake in the form of a rectangular parallelepiped for Fr < 0.1, (B) vortices with a vertical axis of rotation for 0.11 < Fr < 0.27, (C) vortices with a horizontal axis of rotation for 0.27 < Fr < 0.8, and (D) three-dimensional vortices for Fr > 0.8, which agree in part with the results of [2, 3]. However, in contrast to [2, 3], it was found in [4] that the classification of flow regimes depends strongly on Re. For example, the boundaries of the flow regimes obtained at Re = 200 in [4] were found to be strongly shifted as compared with those at Re = 100: (A) Fr < 0.06, (B) 0.06 < Fr < 0.17, (C) 0.17 < Fr < 0.55, and (D) Fr > 0.55. Judging from our experience, a laminar wake in the form of a rectangular parallelepiped (regime A) does not exist. In our computations, there is an oval rather than a rectangle in a vertical cross section perpendicular to the z axis.

For Fr < 0.4, the kinetic energy of some of the impinging fluid particles with vertical coordinates lying between those of the upper pole and center of the sphere turns out to be less than the potential energy required for lifting up to the upper pole [31]. Then these fluid particles continue to move in the neighborhoods of their level around the lateral parts of the sphere. In the case of a long cylinder, these fluid particles cannot bend the cylinder, so they form a recirculation zone blocking the fluid ahead of the cylinder. On the basis of shadow patterns visualizing density gradients, it was concluded in [6, 7] that there is a zone blocking the fluid ahead of the sphere (by analogy with a cylinder) in some range of the parameters of the problem. At the same time, no blocking zone was observed in [2, 3, 11–14].

4. CLASSIFICATION OF SIV FLOW REGIMES AROUND A SQUARE CYLINDER AT Re < 200

Obtained via optimal-grid computations on supercomputers of Joint Supercomputer Center of the Russian Academy of Sciences, our classification of SIV flow regimes around a square cylinder (Fig. 7) [32] is based on the topology of steady streamline patterns and differs fundamentally from the classification of flow patterns in a sphere wake. Six flow regimes were identified: 1RZ, one RZ is observed; V, new vortices are formed periodically in the wake (Fig. 8b); BZ, a blocking zone occurs in front of the cylinder; 2RZ, BZ + RZ (Fig. 8a) (Fr ≈ 0.45 is the boundary between regimes 1RZ and 2RZ); 2RZU, new vortices bounded above and below by internal waves are formed periodically in the wake (Fig. 8c); and 2RZS,

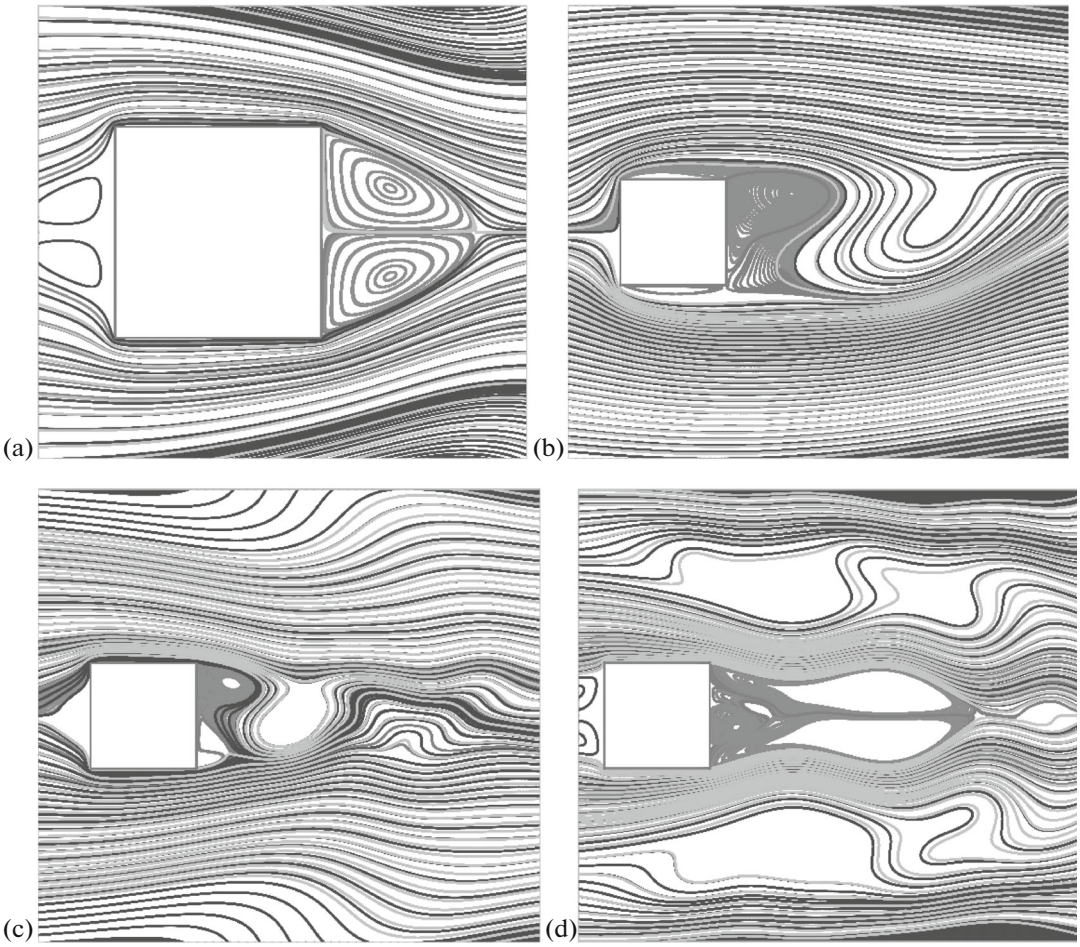

Fig. 8. (a)–(d) Streamlines over the square cylinder at (Fr, Re) = (0.3, 50), (2, 200), (0.4, 200), and (0.2, 200).

unsteady RZ and BZ with a symmetric flow outside RZ and BZ (Fig. 8d) (Fr ≈ 0.37 is the boundary between 2RZU and 2RZS).

At Re = 50 and Fr = 100, integral flow characteristics (such as the length of RZ and the drag coefficient) agree very well with the results of [33]. Qualitatively, the classification of flow regimes behind a two-dimensional square cylinder (Fig. 7) is in good agreement with the classification of flow regimes behind a circular cylinder obtained experimentally in [8]. However, the periodic regime at Fr = 2 begins at Re = 167.5 in our case, while at Re ≈ 100 in [8]. In [8], 2RZU and 2RZS are joined in the single regime C_M (a wake exhibiting several central structures with strong rotors observed above and below them). Additionally, in contrast to Fig. 7, there are no horizontal boundaries between flow regimes in the (Re, Fr) plane in [8]. The classification in [9] takes into account various fine details of the flow, so six flow regimes are identified for Fr > 0.1 and Re < 200 in [9], which differ from our classification in Fig. 7.

5. FORMATION OF SIV FLOW PAST A SQUARE CYLINDER AT Fr = 0.1 AND Re = 50 (Figs. 9–11)

For Fr < 0.37 and Re > 30, two symmetric wavy hanging density layers (Figs. 11a, 11b) are observed in the wake behind the square cylinder. Consider the formation of these layers at Fr = 0.1, Re = 50, and A = 440 after the cylinder starts moving by applying an impulse. First ($T < 4$), the topology of unsteady internal waves in the contour lines of the horizontal density gradient resembles a chamomile with $(8T + 6)$ petals, which corresponds to $(2T + 1.5)$ waves (Fig. 9). Over time, the wake of the cylinder is supplemented with associated internal waves, which occupy progressively more space around the moving body (Fig. 10). Moreover, the instantaneous streamline pattern in the frame of reference tied to the body reveals BZ and

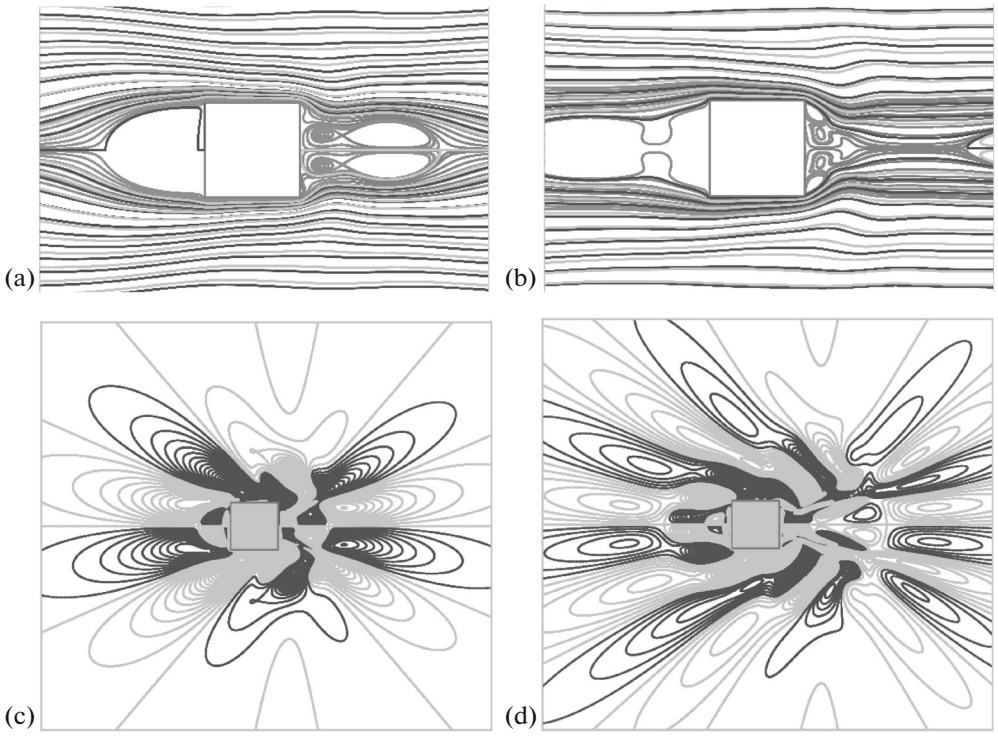

Fig. 9. SIV flow past a square cylinder at Fr = 0.1 and Re = 50: (a, b) instantaneous streamlines at $T = 1$, 2; and (c, d) contour lines of the horizontal density gradient with contour intervals of 6.52×10^{-6} and 6.53×10^{-6} at $T = 1$ and 2, respectively.

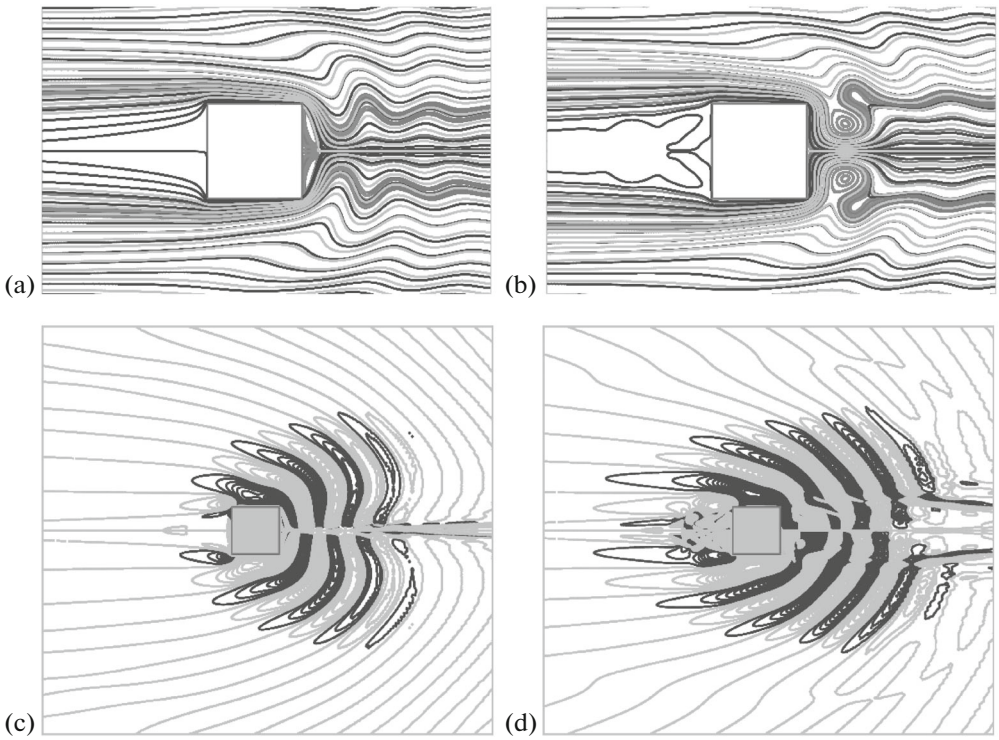

Fig. 10. SIV flow past a square cylinder at Fr = 0.1 and Re = 50: (a, b) instantaneous streamlines at $T = 20$, 100; (c, d) contour lines of the horizontal density gradient with contour intervals of 4.19×10^{-5} and 1.87×10^{-5} at $T = 20$ and 100, respectively.

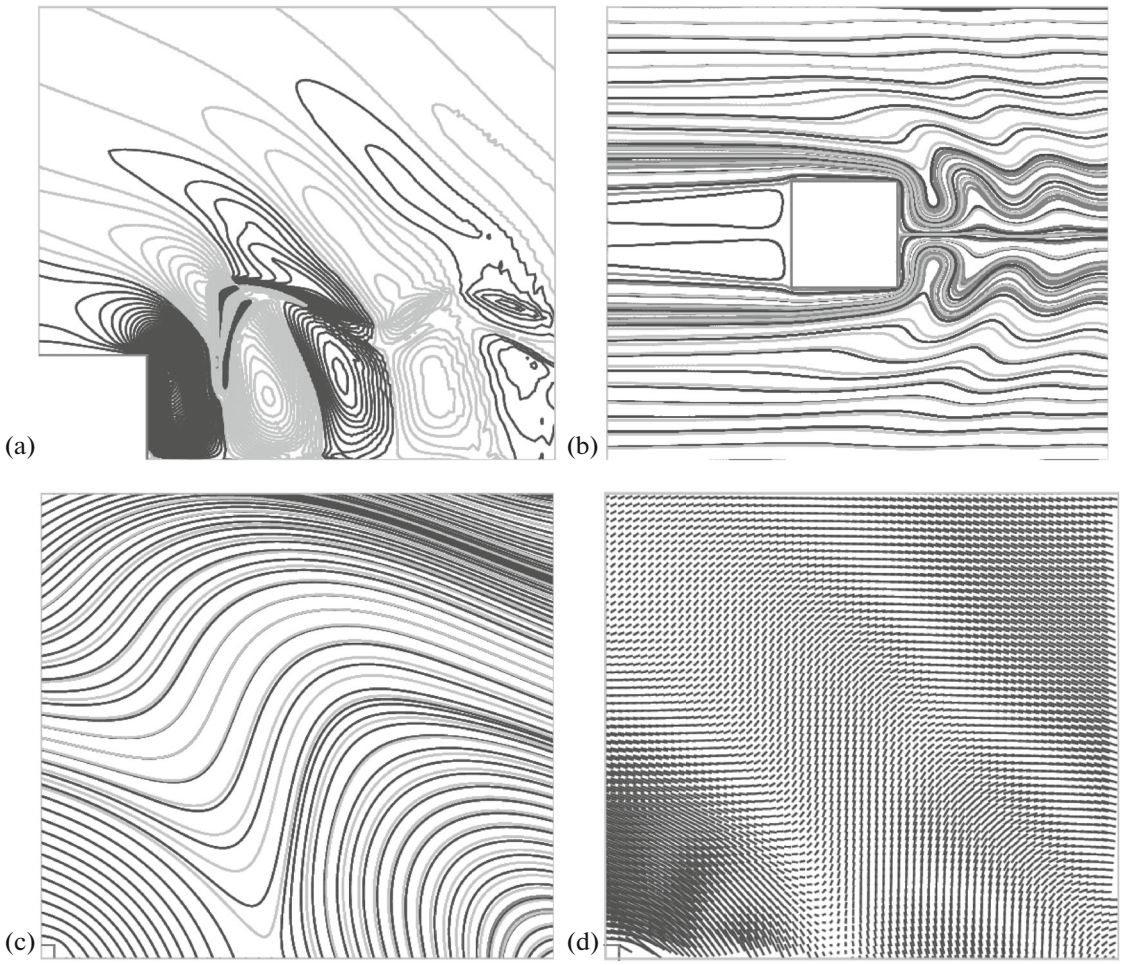

Fig. 11. Steady SIV flow past a square cylinder at Fr = 0.1, Re = 50, $T = 574$: (a) contour lines of the horizontal density gradient with a contour interval of 1.17×10^{-4}; (b, c) streamlines over the square cylinder; and (d) the velocity field multiplied by 0.02. (The same flow region is shown in Figs. 11c and 11d. The upper back corner of the square cylinder is seen in the lower left corner in Figs. 11c and 11d).

RZ, whose sizes vary with time. At $T = 20$, the size of RZ is equal to $d/6$. Next, RZ disappears and, at $T = 100$, two symmetric hanging vortices are formed near the back side of the cylinder (Fig. 10b).

At $T = 574$ (Fig. 11), the flow past the cylinder with two symmetric wavy hanging density layers can be regarded as steady. At $T = 574$, two hanging layers begin not with two symmetric hanging vortices as at $T = 100$, but rather with two symmetric singular points of the velocity field. Flow patterns similar to those in Fig. 11a were observed in shadow patterns (Foucault knife-edge method) obtained experimentally in [10]. Note that the maximum drop in the horizontal density gradient within the region of wavy hanging layers in our computation is very small (roughly equal to 0.01) and is associated with a perfectly smooth velocity field (Fig. 11d), whereas, according to [10], the density drop on hanging layers is very large, the layers themselves are called hanging discontinuities, and the normal velocities on the upper and lower edges of discontinuities differ. Thus, the computations performed refute this doubtful experimental conclusion drawn in [10] by analyzing internal wave fields on shadow patterns (mapping different density gradients) rather than velocity fields themselves.

6. CONCLUSIONS

The previously developed method MERANZH of splitting with respect to physical factors [15, 16] with an explicit hybrid finite-difference scheme (second-order accurate in space, monotone, and having minimum numerical viscosity and dispersion) intended for approximating the convective terms in the Navier–Stokes equations in the Boussinesq approximation was used in direct numerical simulation of lin-

early stratified (in density) incompressible viscous flows behind a sphere and a square cylinder (or prism) moving uniformly in a horizontal direction. For $0.005 < \mathrm{Fr} < 100$, we improved the classification of flow regimes for a sphere ($1 < \mathrm{Re} < 500$) and for a square cylinder ($1 < \mathrm{Re} < 200$). At $\mathrm{Fr} = 0$ (i.e., at $U = 0$), the diffusion-induced flow around a stationary sphere was considered, which leads to the formation of horizontal density layers near the upper and lower poles of the sphere. At $\mathrm{Fr} = 0.1$ and $\mathrm{Re} = 50$, the formation of a steady flow past a square cylinder with wavy hanging density layers developing in the wake was analyzed in detail.

The study of SIV flows around a sphere and a square cylinder showed that, as Fr is decreased from 10 to 1, the buoyancy forces flatten flow structures typical of a homogeneous fluid in both vertical and horizontal directions, make the velocity field symmetric about the horizontal plane passing through the center of the body, and increase the critical Reynolds number (at which the wake flow becomes unsteady). As Fr is decreased further, the flow structure around the body changes substantially, but the velocity field remains symmetric about the horizontal plane in most of the flow region (except for small unsteady domains).

ACKNOWLEDGMENTS

This work was supported by the Russian Foundation for Basic Research (project nos. 14-01-00428, 15-51-50023), by the Presidium of the Russian Academy of Sciences (program no. I.8P), and by the Branch of Mathematics of the Russian Academy of Sciences (program no. IV.1.3).

REFERENCES

1. G. D. Crapper, "A three-dimensional solution for waves in the lee of mountains," J. Fluid Mech. **6**, 51–76 (1959).
2. Q. Lin, W. R. Lindberg, D. L. Boyer, and H. J. S. Fernando, "Stratified flow past a sphere," J. Fluid Mech. **240**, 315–354 (1992).
3. J. M. Chomaz, P. Bonneton, and E. J. Hopfinger, "The structure of the near wake of a sphere moving horizontally in a stratified fluid," J. Fluid Mech. **254**, 1–21 (1993).
4. E. Ya. Sysoeva, Candidate's Dissertation in Mathematics and Physics (Moscow, 1990).
5. E. Ya. Sysoeva and Yu. D. Chashechkin, "Vortex structure of a wake behind a sphere in a stratified fluid," J. Appl. Mech. Tech. Phys. **27** (2), 190–196 (1986).
6. E. Ya. Sysoeva and Yu. D. Chashechkin, "Spatial structure of a wake behind a sphere in a stratified fluid," J. Appl. Mech. Tech. Phys. **29** (5), 655–660 (1988).
7. Yu. D. Chashechkin, "Hydrodynamics of a sphere in a stratified fluid," Fluid Dyn. **24** (1), 1–7 (1989).
8. D. L. Boyer, P. A. Davies, H. J. S. Fernando, and X. Zhang, "Linearly stratified flow past a horizontal circular cylinder," Philos. Trans. R. London Soc. Ser. A: Math. Phys. Sci. **328** (1601), 501–528 (1989).
9. Yu. D. Chashechkin and I. V. Voeikov, "Vortex systems past a cylinder in a continuously stratified fluid," Izv. Atmos. Ocean Phys. **29** (6), 821–830 (1993).
10. V. V. Mitkin and Yu. D. Chashechkin, "Transformation of hanging discontinuities into vortex systems in a stratified flow behind a cylinder," Fluid Dyn. **42** (1), 12–23 (2007).
11. H. Hanazaki, "A numerical study of three-dimensional stratified flow past a sphere," J. Fluid Mech. **192**, 393–419 (1988).
12. P. V. Matyushin, "The vortex structures of the 3D separated stratified fluid flows around a sphere," *Selected Papers of the International Conference on Fluxes and Structures in Fluids 2007* (July 2–5, 2007, Russia), Ed. by Yu. D. Chashechkin and V. G. Baydulov (IPMech. Russ. Acad. Sci., Moscow, 2008), pp. 139–145.
13. P. V. Matyushin, "Continuous transformation of the vortex structures around a moving sphere with increasing of the fluid stratification," *Selected Papers of the International Conference on Flows and Structures in Fluids: Physics of Geospheres 2009* Ed. by Yu. D. Chashechkin and V. G. Baydulov (IPMech. Russ. Acad. Sci., Moscow, 2008), pp. 251–258.
14. V. A. Gushchin and P. V. Matyushin, "Numerical simulation and visualization of vortical structure transformation in the flow past a sphere at an increasing degree of stratification," Comput. Math. Math. Phys. **51** (2), 251–263 (2011).
15. O. M. Belotserkovskii, V. A. Gushchin, and V. N. Konshin, "The splitting method for investigating flows of a stratified liquid with a free surface," USSR Comput. Math. Math. Phys. **27** (2), 181–191 (1987).
16. V. A. Gushchin and V. N. Konshin, "Computational aspects of the splitting method for incompressible flow with a free surface," J. Comput. Fluids **21** (3), 345–353 (1992).
17. V. A. Gushchin and P. V. Matyushin, "Numerical simulation of separated flow past a sphere," Comput. Math. Math. Phys. **37** (9), 1086–1100 (1997).

18. V. A. Gushchin, A. V. Kostomarov, P. V. Matyushin, and E. R. Pavlyukova, "Direct numerical simulation of the transitional separated fluid flows around a sphere and a circular cylinder," J. Wind Eng. Ind. Aerodyn. **90** (4–5), 341–358 (2002).
19. V. A. Gushchin and P. V. Matyushin, "Classification of Regimes of Separated Fluid Flows over a Sphere at Moderate Reynolds Numbers," in *Mathematical Simulation: Problems and Results* (Nauka, Moscow, 2003), pp. 199–235 [in Russian].
20. V. A. Gushchin, A. V. Kostomarov, and P. V. Matyushin, "3D visualization of the separated fluid flows," J. Visualization **7** (2), 143–150 (2004).
21. V. A. Gushchin and P. V. Matyushin, "Mathematical modeling of 3D incompressible fluid flows," Mat. Model. **18** (5), 5–20 (2006).
22. P. V. Matyushin, Candidate's Dissertation in Mathematics and Physics (Moscow, 2003).
23. V. A. Gushchin and P. V. Matyushin, "Vortex formation mechanisms in the wake behind a sphere for $200 < Re < 380$," Fluid Dyn. **41** (5), 795–809 (2006).
24. L. S. Pontryagin, *Ordinary Differential Equations* (Addison- Wesley, Reading, Mass., 1962; Nauka, Moscow, 1974).
25. M. S. Chong, A. E. Perry, and B. J. Cantwell, "A general classification of three-dimensional flow fields," Phys. Fluids A **2** (5), 765–777 (1990).
26. J. Jeong and F. Hussain, "On the identification of a vortex," J. Fluid Mech. **285**, 69–94 (1995).
27. V. G. Baidulov, P. V. Matyushin, and Yu. D. Chashechkin, "Structure of a diffusion-induced flow near a sphere in a continuously stratified fluid," Dokl. Phys. **50**, 195–199 (2005).
28. V. G. Baidulov, P. V. Matyushin, and Yu. D. Chashechkin, "Evolution of the diffusion-induced flow over a sphere submerged in a continuously stratified fluid," Fluid Dyn. **42** (2), 255–267 (2007).
29. K. E. B. Lofquist and L. P. Purtell, "Drag on a sphere moving horizontally through a stratified liquid," J. Fluid Mech. **148**, 271–284 (1984).
30. P. J. Mason, "Forces on spheres moving horizontally in a rotating stratified fluid," Geophys. Astrophys. Fluid Dyn. **8**, 137–154 (1977).
31. P. A. Sheppard, "Air flow over mountains," Q. J. R. Met. Soc. **82**, 528–529 (1956).
32. P. V. Matyushin, "Classification of the regimes of the stratified viscous fluid flows around a 2D square cylinder," *Proceedings of the International Conference on Fluxes and Structures in Fluids* (June 25–28, 2013, Russian State Hydrometeorological University, St. Petersburg) (Maks-Press, Moscow, 2013), pp. 209–212.
33. C. Norberg, A. Sohankar, and L. Davidson, "Numerical simulation of unsteady flows around a square two-dimensional cylinder," *Twelfth Australian Fluid Mechanics Conference* (Univ. of Sydney, Australia, Sydney, 1995), pp. 517–520.

Translated by I. Ruzanova